Carbon Nanotube (CNT) Enhancements for Aerosurface State Awareness

Seth S. Kessler and Christopher T. Dunn
Metis Design Corporation

Sunny S. Wicks, Roberto Guzman de Villoria,
and Brian L. Wardle
Massachusetts Institute of Technology

ABSTRACT

The goal of the present effort was to develop an integrated system capable of reliable ice-detection, de-icing and anti-icing in addition to structural diagnostics to enable aerosurface state awareness. The basis for the system is nanoengineered structured carbon nanotube (CNT) enhancements that can either be embedded within the composite laminates during manufacturing, or applied as a separate surface layer in a secondary process. The aligned CNTs are sufficiently long (20-30 um) to span interply matrix regions, acting as mechanical reinforcement in addition to improving electrical conductivity by a factor of more than a million. Optimized electrode patterns are applied to the CNT-enhanced structure, and hardware provides closed-loop feedback control. Ice-detection is based on effective heat capacity, where power is applied to CNT-enhanced laminates (termed fuzzy fiber reinforced plastic, or FFRP) for seconds, and the slope of the temperature rise can be correlated to the thickness of ice present. For de-icing (melting) and anti-icing (prevention of ice formation) a resistive heating principal is used. Voltage is applied to the FFRP material, which heats rapidly due to the small but finite resistance imparted by the CNTs. Structural diagnostics is achieved by monitoring and mapping changes in electrical resistance across electrode grid paths.

INTRODUCTION

Advanced composite materials are being adopted increasingly in aerospace structure design, including aero-surfaces, due to their superior specific stiffness and strength, as well as their resistance to fatigue, corrosion and ability to greatly reduce part count. Composites present additional challenges for inspection however, due

Seth S. Kessler, Metis Design Corporation, 10 Canal Park, Cambridge, MA 02141
Christopher T. Dunn, Metis Design Corporation, 10 Canal Park, Cambridge, MA 02141
Sunny S. Wicks, Massachusetts Institute of Technology, Cambridge, MA 02139
Roberto Guzman de Villoria, Massachusetts Institute of Technology, Cambridge, MA 02139
Brian L. Wardle, Massachusetts Institute of Technology, Cambridge, MA 02139

to their heterogeneity and anisotropy, and the fact that damage can occur beneath the visible surface. Currently successful laboratory non-destructive testing methods are impractical for service inspection of large-area integrated composite structures due to the size and complexity of the support equipment required. Furthermore, as with traditional aero-surfaces, ice accumulation can result in reduced lift and increased drag, therefore the presence of ice must be explicitly monitored as well.

Several studies have shown that carbon nanotubes (CNTs) possess exceptional mass-specific properties such as mechanical stiffness (as high as ~1 TPa) and strength, as well as excellent electrical conductivity and piezoresistivity (resistivity change with mechanical strain) [1-18]. A novel approach to incorporating *aligned* CNTs grown *in situ* in fiber-reinforced aerospace structural composites for SHM was developed [21], which can fully exploit all the potential advantages of CNTs for improving mechanical properties [20, 21] as well as enable SHM with a non-invasive electrode network. Laminates developed through MIT's Nano-Engineered Composite Aerospace STructures (NECST) consortium have already been demonstrated to have as high as 69% higher interlaminar shear strength and much greater electrical conductivity (10^8 through-thickness & 10^6 in-plane) compared to similar laminates without CNTs [20]. They consist of a three-part hybrid system: advanced fibers (diameter of order microns) organized in tows and woven, a thermoset polymer resin, and dense aligned CNTs (with volume fraction between 1.0 and 3%) organized within the polymer matrix. As illustrated in Figure 1, CNTs are organized radially around the existing micron-sized fibers, and the polymeric matrix binds all the filaments (nano-scale dia. CNTs and micron-scale dia. advanced fibers) together. The alignment of CNTs within the dense array of woven tows and fibers in the cloth material is achieved by radial *in situ* growth of CNTs from the surface of the woven fibers. The CNTs reinforce the polymer matrix between the advanced fibers to provide enhanced strength and toughness, as well as electrically conductive pathways.

Furthermore, it has recently been demonstrated that due to the combined thermal and electrical properties of the CNTs, that by applying a small voltage across electrodes, these laminates can rapidly heat up [22]. A proof of concept experiment was conducted by the present investigators to demonstrate the ability to easily melt an ice layer covering a composite beam within seconds. By combining this technology with a previously developed direct write electrode grid, a standalone system will be able to achieved capable of monitoring impact damage, ice build-up, and selectively anti/de-icing with closed loop voltage feedback to control temperature between electrode pairs.
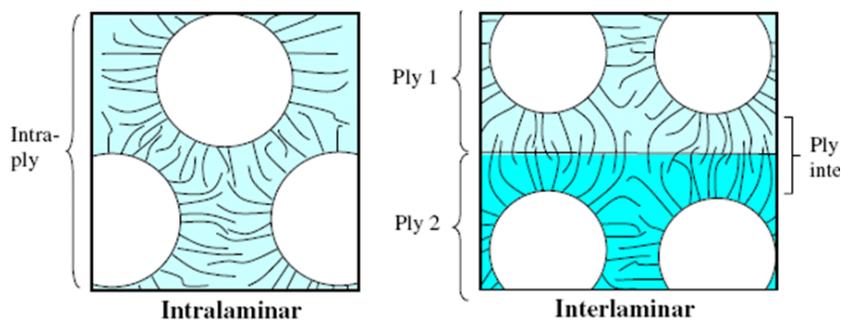
Figure 1: Illustration of fuzzy fiber reinforced plastic (FFRP) developed at MIT [20].

APPROACH

Ice-detection is achieved based on effective heat capacity, where a step-function of power is applied to the CNT through DW electrodes for a very brief period (seconds), and temperature rise is recorded. The slope of that rise can been well correlated to the thickness of ice present on the surface. For de-icing (melting) and anti-icing (prevention of ice formation) a resistive heating principal is used. A voltage applied the FFRP will heat the blade due to the small but finite resistance of the laminate. Due to enhanced FFRP thermal conductivity, heat will be distributed relatively evenly along the blade surface. Optimal power can be achieved depending on the desired melt time and steady-state blade temperature (ie how far above 0°C).

Experimental Setup

As can be seen in Figure 2, the nanoengineered FFRP specimen is approximately $115 \times 25 \times 2$ mm. Thirty-two vertical electrodes on top and eight horizontal electrodes on the backface were printed using a direct write process similar to silk screening. The electrodes were comprised of silver epoxy. Bonded to the FFRP sample is a flex circuit which allows for electrical connection to either end of any of the silver electrodes. The flex circuit has two connectors that mate with flat flexible cables. The sample was sprayed with liquid electrical tape for moisture protection, and taped to a nylon plate for ease of handling and strain relief. Two 18 AWG wires were soldered to the flex circuit, connecting the vertical traces on either extreme of the sample, yielding a total system resistance of 1.34 Ω. One surface mount K-type thermocouple was mounted to the center of the CNT sample and a second thermocouple was mounted ~15 cm to the left of the center of the sample. To heat the sample, electrical power was applied using a DC power supply. Finally, a vacuum tape frame was assembled around the FFRP sample so that water could be poured into the frame without leaking onto the electrodes. Separate logging multimeters were used to monitor temperature and current.
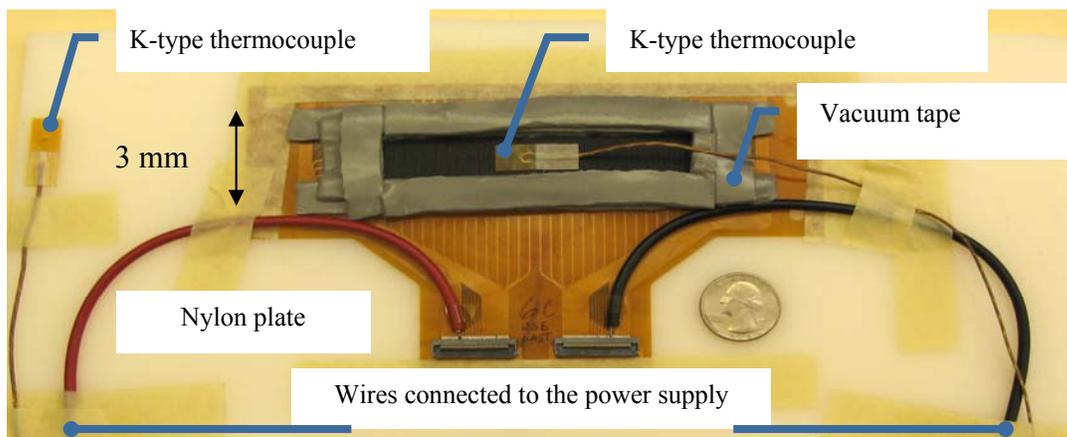
Figure 2: Nanoengineered FFRP laminate experimental setup for ice experiments.

Ice Detection

Consider a solid (such as the FFRP laminate) comprised of n discrete materials immersed in a fluid of temperature T_0. The body is heated by volumetric heating and cooled by convective heat transfer. Placing a control volume around the system, the energy flow is given by the first law of thermodynamics:

$$\dot{E}_{in}(t) + \dot{E}_{gen}(t) = \dot{E}_{sto}(t) + \dot{E}_{out}(t) \tag{1}$$

where t is time, $\dot{E}_{in}(t)$ is the rate of energy entering the control volume, $\dot{E}_{gen}(t)$ is the rate of energy generated within the control volume, $\dot{E}_{sto}(t)$ is the rate of energy stored within the control volume, and $\dot{E}_{out}(t)$ is rate of energy leaving the control volume. Let us assume that no energy is entering the control volume except through volumetric heating:

$$\dot{E}_{in}(t) = 0 \qquad \dot{E}_{gen}(t) = \int_V Q(\vec{x},t)dV \tag{2}$$

where Q is the volumetric heating rate and $\vec{x}$ is the position. If no phase transitions occur within the control volume, the rate of energy stored is:

$$\dot{E}_{sto}(t) = \int_V \rho c \frac{dT(\vec{x},t)}{dt}dV \tag{3}$$

where ρ is the mass density, and c is the specific heat per unit mass, and T is temperature. The rate of energy leaving the control volume is given by:

$$\dot{E}_{out}(t) = \int_A \vec{q}(\vec{x},t) \cdot \vec{n}(\vec{x})dA \tag{4}$$

where q is the heat flux vector, and n is the outward normal vector. If heat is lost only through convection, the normal heat flux is given by:

$$\vec{q}(\vec{x},t) \cdot \vec{n}(\vec{x}) = h(\vec{x})[T(\vec{x},t) - T_0] \tag{5}$$

where h is the convection coefficient. The system is initially at thermal equilibrium with ambient conditions. At time zero, a constant electrical power P is applied to the body to heat it. Thus the rate of energy generated within the control volume equals the input electrical power:

$$\dot{E}_{gen}(t) = P \tag{6}$$

Let us assume for the moment that the n materials are infinitely conducting, and therefore the temperature of the body is independent of position.

$$T(\vec{x},t) = T(t) \tag{7}$$

Also, let us assume that that the convection coefficient, density, and specific heat are dependent only on the material number. With these assumptions, the rate of stored and output energy terms, Equations 3 and 4, are given by:

$$\dot{E}_{sto}(t) = \left[\sum_{i=1}^{n} \rho_i c_i V_i\right]\frac{dT(t)}{dt} \qquad \dot{E}_{out}(t) = \left[\sum_{i=1}^{n} h_i A_i\right](T(t) - T_0) \tag{8}$$

Where i subscript indicates the parameter is for the ith material. Materials internal to the body have a convection coefficient of zero since integration in Equation 4 is

performed over the control area. It should be noted that the mass of material i is given by:

$$m_i = V_i\, \rho_i \qquad (9)$$

Solving Equation 1 for temperature, and using Equations 6 - 9:

$$T(t) = T_0 + P\left(1 - e^{-t\lambda}\right) \bigg/ \sum_{i=1}^{n} h_i\, A_i \qquad (10)$$

where the exponential decay constant λ is given by:

$$\lambda = \sum_{i=1}^{n} h_i\, A_i \bigg/ \sum_{i=1}^{n} m_i\, c_i \qquad (11)$$

It should be noted that the derivative of the temperature at time equal zero is given by:

$$\left. \frac{dT}{dt} \right|_{t=0} = P \bigg/ \sum_{i=1}^{n} m_i\, c_i \qquad (12)$$

Note that Equation 12 is independent of the convection coefficient. Thus, two samples with different convection boundary conditions will have the same initial slope, assuming the same power is applied. Consider two bodies starting at temperature T_0 and heated with power P. The first body has n materials, and the second body has $n+1$ materials. The ratio of the initial slope is given by:

$$\frac{\left. \dfrac{dT}{dt} \right|_{t=0} (n\,\text{materials})}{\left. \dfrac{dT}{dt} \right|_{t=0} (n+1\,\text{materials})} = \frac{P}{\displaystyle\sum_{i=1}^{n} m_i\, c_i} \cdot \frac{\displaystyle\sum_{i=1}^{n+1} m_i\, c_i}{P} = 1 + \frac{m_{n+1}\, c_{n+1}}{\displaystyle\sum_{i=1}^{n} m_i\, c_i} \qquad (13)$$

Since the specific heat and mass are greater than zero for all materials, the ratio in Equation 13 is greater than one. Thus the slope decreases as an additional material (such as ice or water) is added to the body. This can be used as a detection scheme to determine if material (water, ice in this case) has been added to the system.

To illustrate the detection of ice using the effective heat capacity principal, the temperature rise for specimens as a function of ice thickness and ambient test temperature was recorded for the first thirty seconds of data with three repetitions of each condition. Data from these tests are presented for the -15 °C ambient condition in Figure 6. From 0 to 20 seconds, the temperature appears nearly linear, and the slope of this line as a function of water depth is shown in Figure 3. For all samples without ice, the temperature rate is above 0.5 °C / sec, however, as the ice thickness increases the temperature increase rate decreases regardless of test temperatures, as predicted by Equation 13. Based upon the prediction of Equation 13 and the data from all the experiments, a simple ice detection algorithm was implemented, similar to that used in differential scanning calorimetry (DSC). In the ice detection algorithm, a constant power is supplied, and the temperature as a function of time is recorded.
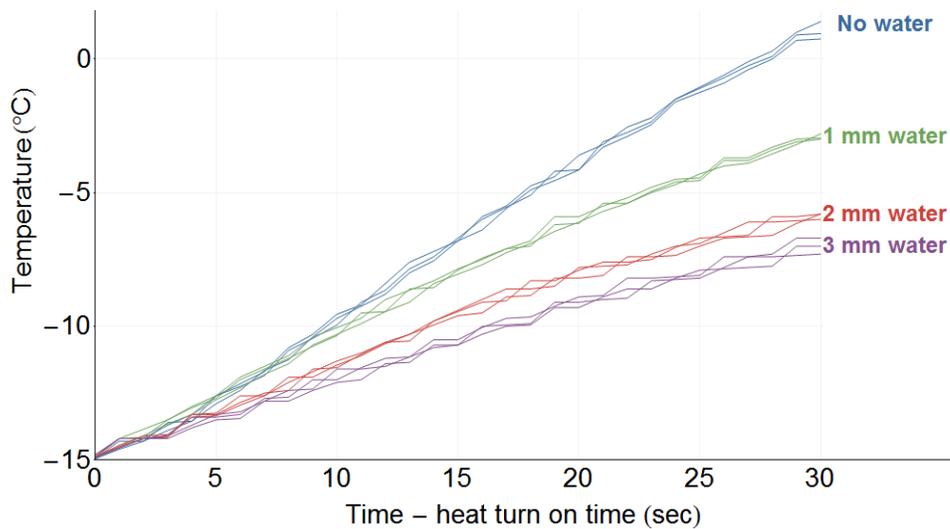
Figure 3: Temperature versus time for the anti-icing tests.

Anti-Icing

To determine the power required to prevent icing, various levels of power were applied to the CNT sample to determine their steady state temperature. Since the Equations predict steady state temperature is the same regardless of the presence of water/ice (only the time constant to achieve steady state is effected) in agreement with intuition, specimens without water were placed in the freezer and allowed to cool to -15 °C. The DC power supply was turned on, and the sample was allowed to heat for thirty minutes. The power was then increased and another thirty minutes of data was collected for a total of 10 power values. The temperature vs. power and power vs. applied voltage appeared nearly linear. The anti-icing power was found to be 2 W including a small margin (steady state value of ~3 °C). The anti-icing power was applied to a specimen with 2.8 g of water for three validation tests, starting at 5 °C following cool down from room temperature, as shown in Figure 4.
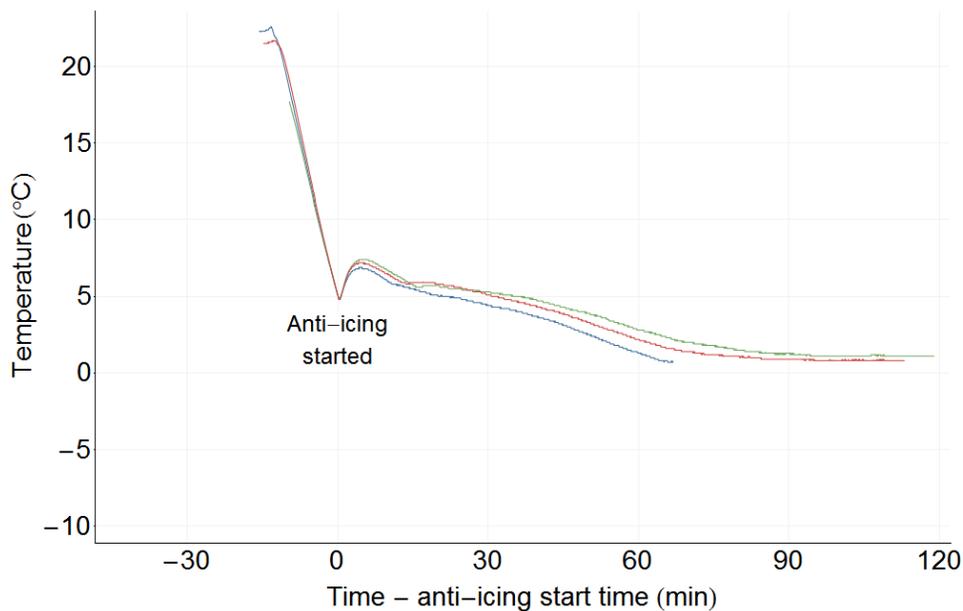
Figure 4: Anti-icing starting from 5 °C following cool-down from room temperature.
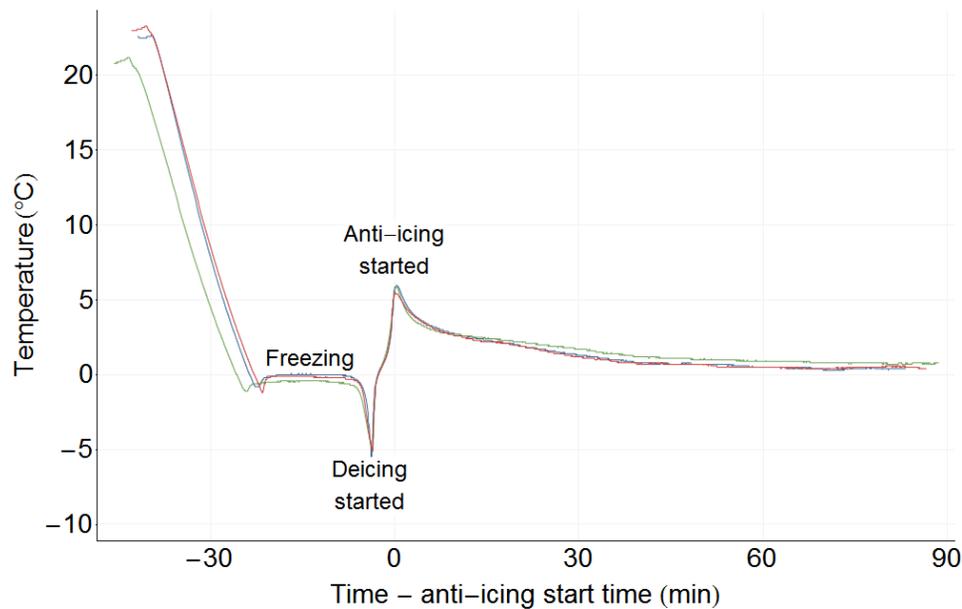
Figure 5: Anti-icing starting from 5 °C following de-icing heat-up from -5 °C,

De-Icing

Tests were performed to determine the FFRP laminate heating rates as a function of ice thickness and ambient temperature. Of particular interest was the de-icing time, or specifically the time to reach 0 °C and subsequently 5 °C (as a safety margin). Tests were performed for water depths of 0, 1, 2, and 3 mm with start temperatures of -5, -10, and -15 °C, with results shown in Figure 5 for -5 °C starting temperature (in this case followed by anti-icing). As the depth of the water increased the initial slope decreases, as predicted by Equation 13. The three tests appear to be very repeatable below freezing, with some scatter above freezing.

CONCLUDING REMARKS

Proof-of-concept experiments were conducted for the detection of ice, anti-icing and de-icing, leading to a full prototype system demonstration. This novel method is comprised of embedded CNTs grown radially aligned in situ on the composite host structure, and silver nano-ink direct write electrode patterned on the host structure surface. Ice detection was conducted via effective heat capacity, while anti-icing and de-icing was achieved by using the nanoengineered FFRP laminate as efficient resistive heaters. The specimen used for these experiments had also been previously used for an impact detection demonstration using the electrode grid to measure changes in local resistivity. The overall system performance was demonstrated and offers many benefits over current ice detection and de-icing systems, including heaters and sensors that are structural, being conformal and uniform, and enabling closed-loop operation. Compared to the conventional resistive heating blanket approach for de-icing, the CNT-enhanced system is more efficient (requires less power), is lighter weight, lower profile, and provides integral system and damage detection feedback.

ACKNOWLEDGMENTS

REFERENCES

1. Treacy M.M.J., Ebbesen T.W. and Gibson T.M., "Exceptionally high Young's modulus observed for individual carbon nanotubes," Nature, v. 381, pp. 680-687, 1996
2. Salvetat J.P., Briggs G.A.D., Bonard J.M., Bacsa R.R., Kulik A.J. and Stockli T., "Elastic and shear moduli of single-walled carbon nanotube ropes," Physical Review Letters, v. 82(5), 944-947, 1999
3. Yu M.F., Lourie O., Dyer M., Moloni K. and Kelly T., "Strength and breaking mechanism of multi-walled carbon nanotubes under tensile load," Science, v. 287, pp. 637-640, 2000
4. Thostenson E.T., Ren Z. and Chou T.-W., "Advances in the science and technology of carbon nanotubes and their composites: a review," Composite Science and Technology, v. 61, pp. 1899-1912, 2001
5. Wei B.Q., Vajtai R. and Ajayan P.M., "Reliability and current carrying capacity of carbon nanotubes," Applied Physics Letters, v. 79, pp. 1172-4, 2001
6. Zhang W., Suhr J. and Koratkar N., "Carbon nanotube/polycarbonate composites as multifunctional strain sensors," Journal of Nanoscience and Nanotechnology, v. 6, pp. 960-4, 2006
7. Dharap P., Li Z.L., Nagarajaiah S. and Barrera E.V., "Nanotube film based on single-walled carbon nanotube for strain sensing," Nanotechnology, v. 15, pp. 379-82, 2004
8. Ajayan P.M. and Tour J.M., "Nanotube composites," Nature, v. 447, pp. 1066-8, 2007
9. Schulte K. and Windle A.H., Editorial, Composite Science and Technology, v. 67, pp. 777, 2007.
10. Garcia, E.J., Wardle, B.L., and A.J. Hart, "Joining Prepreg Composite Interfaces with Aligned Carbon Nanotubes," *Composites Part A*, Vol. 39, 2008, pp. 1065-1070.
11. Gojny F.H., Wichmann M.H.G., et al., "Carbon nanotube-reinforced epoxy composites: enhanced stiffness and fracture toughness at low nanotube content," Composite Science & Technology, v. 64, pp. 2363-71, 2004
12. Veedu V.P., Cao A., Li X., Ma K, Solano C., Kar S. et al., "Multifunctional composites using reinforced laminae with carbon-nanotube forests," Nature Materials, v. 5, pp. 457-62, 2006
13. Beyakrova E., Thostenson E.T., Yu A., Kim H., Gao J., Tang J. et al., "Multiscale carbon nanotube-carbon fiber reinforcement for advanced epoxy composites," Langmuir, v. 23, pp. 3970-4, 2007
14. Zhu J., Imam A., et al., "Processing a glass fiber reinforced vinyl ester composite with nanotube enhancement of interlaminar shear strength," Composite Science & Technology, v. 67, pp. 1509-17, 2007
15. Yi Y.B., Berhan L., Sastry A.M., "Statistical geometry of random fibrous networks, revisited: waviness, dimensionality, and percolation," Journal of Applied Physics, v. 96(3), pp. 1318-27, 2004
16. Du F.M., Fischer J.E., Winey K.I., "Effect of nanotube alignment on percolation conductivity in carbon nanotube/polymer composites," Physical Review B, v. 72(12), pp. 121404, 2004
17. Thostenson E.T. and Chou T.-W., "Carbon nanotube networks: sensing of distributed strain and damage for life prediction and self healing," Advanced Materials, v. 18, pp. 2837-41, 2006
18. Chou T.-W., Li C., and E.T. Thostenson. "Sensors and Actuators Based on Carbon Nantubes and Their Composites: A Review," Composites Science and Technology, 68(6) 1227-1249 (2008).
19. Wicks, S., Raghavan, A., Guzmán de Villoria, R., Kessler, S.S., and B.L. Wardle, "Tomographic Electrical Resistance-based Damage Sensing in Nano-Engineered Composite Structures," AIAA-2010-2871, *51st AIAA Structures, Structural Dynamics, and Materials (SDM) Conference*, Orlando, FL, April 12-15, 2010.
20. Garcia E.J., Wardle B.L., Hart J.A. and Yamamoto N., "Fabrication and multifunctional properties of a hybrid laminate with aligned carbon nanotubes grown in situ," Composite Science and Technology, v. 68, pp. 2034-41, 2008.
21. Wicks, S.S., Guzmán de Villoria, R., and B.L. Wardle, "Interlaminar and Intralaminar Reinforcement of Composite Laminates with Aligned Carbon Nanotubes," *Composites Science and Technology*, 70 (2010), pp. 20–28.
22. Guzmán de Villoria, R., Yamamoto, N., Miravete, A., and B.L. Wardle, "Multi-Physics Damage Sensing in Nano-Engineered Structural Materials," online in *Nanotechnology*, April 2011.